The Crustal Anisotropy of West Ordos Block and Its Geodynamic Implications

Jinyu Lv[1,2], **Xuzhang Shen**[1,2] , **Liuting Huang**[1,2], **Xiaohui He**[1,2], **He Huang**[1,2] , **Wenjun Zheng**[1,2] , **Dongli Zhang**[1,2], and **Jian Zhang**[1,2]

[1]Guangdong Provincial Key Lab of Geodynamics and Geohazards, School of Earth Sciences and Engineering, Sun Yat-Sen University, Guangzhou, China, [2]Southern Marine Science and Engineering Guangdong Laboratory (Zhuhai), Zhuhai, China

Abstract Based on the teleseismic records of the dense broadband seismic array, the crustal anisotropy parameters of the west Ordos block and its adjacent regions were determined with P wave receiver functions. The results indicate that the dominant direction of the fast wave is NEE-SWW, N-S in Yingshan block and north Ordos block, N-S in the south Ordos block, and E-W in the Qinling–Dabie orogen belt. The fast wave direction of crustal anisotropy in the north Ordos block is distinctly different from that in the south Ordos block, both well related to the major geological events, such as the Paleoproterozoic continent-to-continent collision between the Ordos Block and the Yinshan Block, the collision between the Western Block and Eastern Block of the North China Craton and the material migration from the Tibetan plateau in Cenozoic. Our results indicate that the crustal anisotropy in the Ordos block preserves the traces of ancient tectonic movements. Combining the results of previous geophysical studies, we presented a crust-mantle interaction model to explain the geophysical observations. The most prominent features of the model are the horizontal eastward expansion of the mantle material in the southern Ordos and the vertical upwelling of the mantle material in the northern Ordos. The different modes of movement of the mantle material led to the deep contrasting structures of north and south Ordos, including the crustal anisotropy. The mantle upwelling also implies that the north Ordos block might be currently experiencing craton destruction.

Plain Language Summary The Ordos block was stable without strong tectonic activity and showed rigid movement characteristics, which has been interpreted as a typical craton. However, some of the new results from geophysics showed that the crust of the Ordos block is not a single and stable structure with an evident low-velocity layer within the crust, strikingly high Poisson's ratio in the north Ordos block, and a low-velocity anomaly in the mantle in the north Ordos, which indicated that the interior of the Ordos is no longer a stable block, and also laid a good foundation further to explore the deep dynamic process of this area. Here, we constrain the crustal anisotropy by the teleseismic records of the dense broadband seismic array in the west Ordos block and its adjacent regions. The results indicated the contrasting structures beneath north and south Ordos blocks, which implied different movements of the mantle material.

1. Introduction

The Ordos block is located in the central part of the North China Craton, and has experienced a complex geodynamic process during the long term of geological evolution. There are three important ancient geological boundaries around Ordos block as shown in Figure 1. The first one is the Khondalite belt (or Inner Mongolia Suture Zone) along the northern boundary of Ordos block. It was formed through the collision between the Ordos and the Yinshan blocks at ~1.95 Ga, to form the Western block (Figure 1; H. L. Guo et al., 2017; Wan et al. 2020; X. Wang et al., 2019; Yin et al., 2011; Zhao & Zhai, 2013). The second one is the Trans-North China Orogen (TNCO) resulted from the ~1.85 Ga collision between Western and Eastern blocks to form the uniform basement of the North China Craton (NCC; Zhao & Zhai, 2013). The third boundary is the Qinling–Dabie orogen (or Central China Orogen) caused by the collision between the NCC and the South China Craton in the Triassic (S. Li et al., 1993; Wu et al., 2009), which also experienced a multistage orogenic evolution with accretion and collision between discrete continental blocks (Y. P. Dong & Santosh, 2016; W. P. Li et al., 2014).
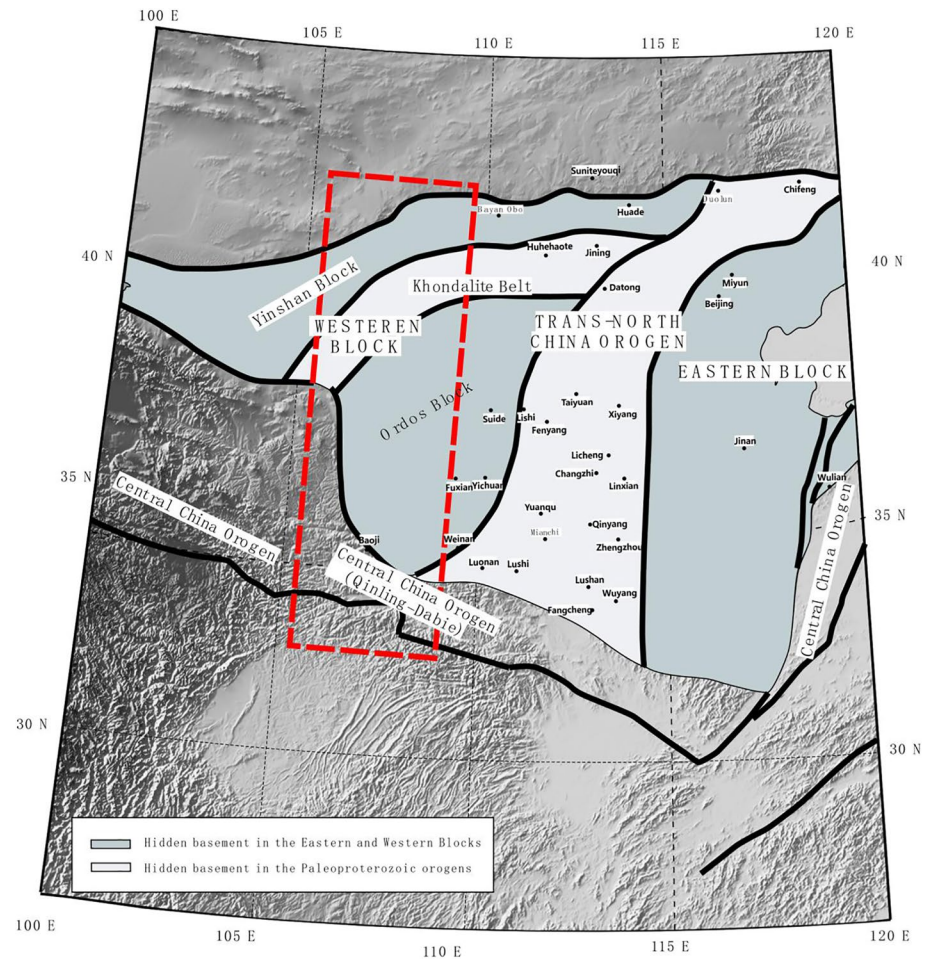
Figure 1. Tectonic background map of the study area. The black lines represent the block boundary and the red box represents the study area.

The current Ordos block has a thick mantle root, no earthquakes, low heat flow, and a lack of internal deformation since the Precambrian (Deng et al., 1999; Gan et al., 2007; B. Guo et al., 2004; S. X. Jia et al., 2014; Kusky, 2011; S. L. Li et al., 2002), which shows that the Ordos block conforms to the characteristics of the craton's stable crust. With the accumulation of high-density and high-quality broadband digital seismic data, some high-resolution and high-precision imaging of the crust, upper mantle, and even deeper interior structures were obtained. Some of the results, however, showed that the crust of the Ordos block is not a single and stable structure. For example, wide-angle reflection and refraction results indicated an evident low-velocity layer at a depth of 20 km in the north Ordos block (M. Jia et al., 2015). H. Dong et al. (2014) found a low resistivity anomaly from the upper mantle to the mid-to-lower crust beneath the northern part of Ordos with a three-dimensional magnetotelluric (MT) inversion. Based on the observations from a dense broadband seismic array, W. L. Wang et al. (2017) obtained the Poisson's ratio using the h–κ stacking method showing a strikingly high Poisson's ratio in the north Ordos block. Tomographic images also show a low-velocity anomaly in the north Ordos, at the upper mantle (H. L. Guo et al., 2017; Zhang et al., 2018). These results supported the regional modification of the lithosphere under the north Ordos and lithosphere thinning beneath Hetao Graben (H. Dong et al., 2014), and also laid a good foundation to explore further the deep dynamic process of this area.

Seismic anisotropy in the crust and mantle is considered a geophysical indicator of the structure and dynamic processes in the Earth's deep interior (Silver, 1996). The direction of the anisotropic fast axis wave is closely related to the direction of material migration, the orientation arrangement of a crystal lattice, and the deformation history during the tectonic evolution. Therefore, the results of seismic anisotropy could be

used to reveal information regarding the geodynamic process. Shear wave splitting measured on the SKS phase is a classical method to determine the anisotropy that has occurred on the upward ray path through the mantle between the core-mantle boundary and the surface on the receiver side. However, SKS splitting is nearly always interpreted in terms of upper mantle anisotropy, and a potential contribution from the lower mantle is mostly ignored (Long & Silver, 2009; Savage, 1999). Receiver functions are another valid method to measure the crustal anisotropy by analyzing the arrival time and polarity of P-to-S converted waves caused by the interfaces of the radial and tangential components. Many research works have been carried out to constrain the crust and the uppermost mantle anisotropy with receiver functions (Bar et al., 2019; Brownlee et al., 2017; Frederiksen & Bostock, 2010; Long, 2013; Mccormack et al., 2013).

Many scholars have studied the crust and mantle anisotropy along the northeastern margin of the Tibetan Plateau and the Ordos block and discussed the deep dynamic process. Yu and Chen (2016) analyzed the seismic anisotropy of the southern Ordos block and the Qinling–Dabie orogenic belt based on the SKS wave splitting and proposed that the belt had an eastward mantle material migration channel response to the horizontal expansion of the Tibetan Plateau. Chang et al. (2017) analyzed the anisotropy of the upper mantle in the Ordos block with the XKS wave splitting and determined that the direction of the anisotropic fast axis inside the Ordos block is near the N-S direction in the north, and near the E-W direction in the south. Z. Huang et al. (2008) discussed the formation mechanism of the anisotropy along on the southern edge of the Ordos block using the S-wave splitting method and proposed that the Ordos block had a counterclockwise rotation trend. The previous anisotropy results for in the Ordos block are mainly from the XKS (SKS, SKKS, and PKS) splitting and have obtained the migration of the upper mantle materials. Shen et al. (2015) documented a low-velocity anisotropic layer in the lower crust in the northeastern margin of the Tibetan Plateau based on the radial and tangential components of a receiver function. These results give important information about the deep dynamic process in the Ordos block and its adjacent regions; however, the previous researches about the crustal anisotropy in Ordos block is still limited, although it would be helpful to understand the deep geodynamic process.

In this paper, the crustal anisotropy parameters were constrained using P wave receiver functions from dense broadband seismic array covering the west Ordos block, part of the Yinshan block, and the Yangtze block as shown in Figure 1. Referring to the previous seismic results, we have discussed the tectonic significance and deep dynamic process of the western Ordos.

2. Observations and Method

During 2013–2016, the dense broadband seismic array, Chin Array-Himalaya II, was set up in the northeastern margin of the Tibetan Plateau by the institute of geophysics of China Earthquake Administration (W. L. Wang et al., 2017). This study used the waveforms of teleseismic earthquakes from 88 temporary broadband stations of the Chin Array-Himalaya II in the west Ordos block and its adjacent regions (Figure 2a). The distribution of the stations was a north-south section with a uniform and good coverage from the Yangtze block to the Alxa block across the Ordos block. The massive observations might ensure obtaining high-quality receiver functions and good constraints of the deep structures.

During the work of the seismic array between September 2013 and June 2016, the teleseismic records of surface-wave magnitude (Ms) $\geq$ 5.5 with epicenter distances in the range of 30°–90° range were selected; the distribution of seismic events is shown in Figure 2b. The original records of the three components (N-E-Z) of the original data were rotated to radial (R), tangential (T), and vertical (Z) components. The three-component records were cut in the time windows of 20 s prior to and 120 s after the P arrival. Receiver functions were calculated by deconvolving the vertical component from the radial and tangential components, respectively, using an iterative approach (Ligorria & Ammon, 1999). A low-pass Gaussian filter with a half-width constant of 1.0 was applied to regulate the deconvolution. Moveout correction was then applied for a reference slowness of 6.4 s/° to correct the influence of different distances. Furthermore, we constructed binning stacks of the R component of receiver functions (RRFs) and T component of receiver functions (TRFs) for each of the stations in an azimuth interval of 6°.

The seismic anisotropy parameters can be represented by the fast direction (FD) and split time (δt; Crampin, 1987; Silver & Chan, 1991). When the P wave passes through the isotropic medium layer, there is no
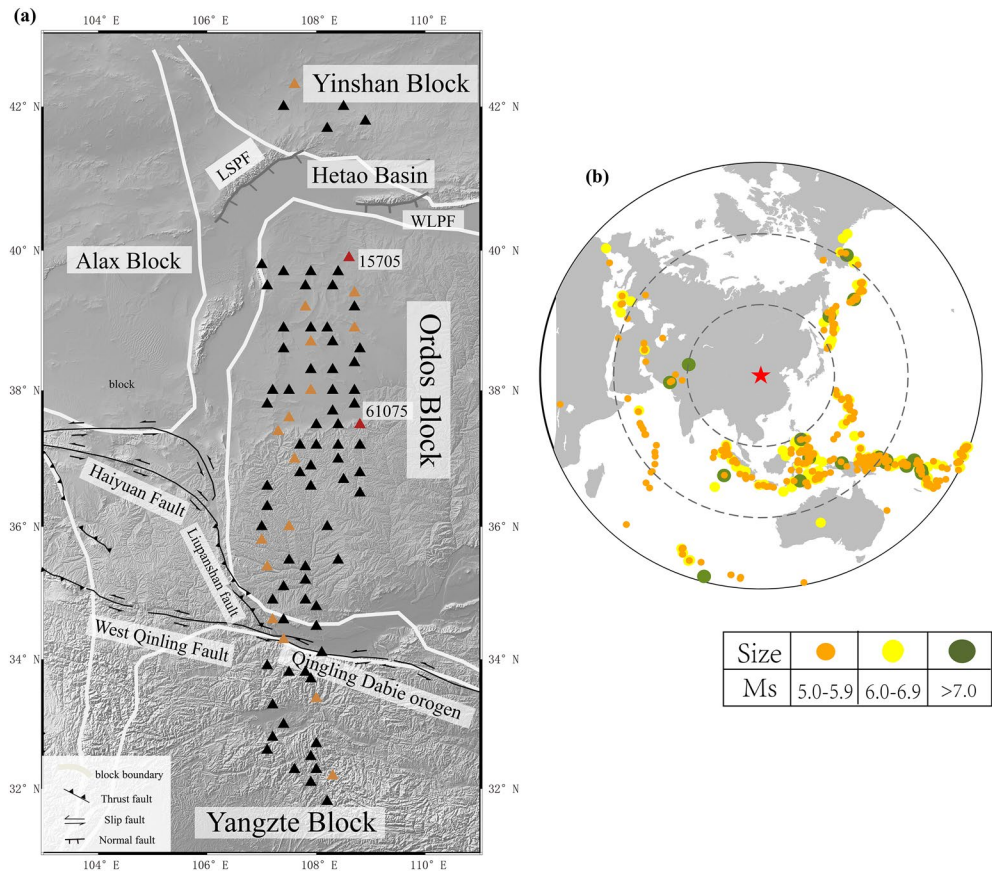
Figure 2. Map of the research area and stations. (a) Distribution of seismic stations. The triangle represents the station position, and white lines represent the block boundary. The receiver functions of the stations with a red triangle are shown in Figures 3 and 4. The station with a black triangle represents stations with periods rule of π for the P_MS arrival in radial receiver functions. The station with a yellow triangle represents the kind of stations with periods rule of 2π for the P_MS arrival in radial receiver functions. LSPF: Lang Shan Piedmont normal fault; WLPF: Wula shan Piedmont normal fault. (b) Epicenters distribution of earthquake events. The red star indicates the central location of the study area.

energy on TRFs. In addition, the arrival P-to-S(P_MS) conversions on RRFs from the Moho with different back azimuth are the same. For the anisotropic layered crust, the incoming P wave splits into a fast and a slow component, causing the azimuth-dependent of arrivals of P_MS on RRFs and the polarity reversal on the TRFs. The TRF exhibit significant azimuthal variation and polarity reversal. In the previous studies, we used the time variations of the P_MS conversions from the Moho in the RRFs and the azimuth-weighted stacking of TRFs (AWST) to determine the fast direction and the magnitude of the anisotropy (delay time) and obtained the anisotropic low-velocity layer in the lower crust beneath the northeastern margin of the Tibetan Plateau (Shen et al., 2015). Here, the same method was applied to the observations to constrain the anisotropic parameters in the western Ordos block. In the following paragraphs, we present the results of two typical stations to describe the method briefly.

Station 61075 is a kind of station with π periodicity of arrivals of P_MS against back azimuth, implying a single layer of anisotropy with a horizontal symmetry axis. We selected 158 RRFs and TRFs to construct the binning stacks in a back azimuth interval of 6° (Figures 3a and 3c). Figure 3b indicates the zoomed time window to highlight the arrival times (green plus symbols) of the P_MS on RRFs (Figure 3a). We obtained the FD and the delay time by fitting the observed arrivals of P_MS. In addition, the TRFs show the periodic rule of π around the arrival time of P_MS (Figure 3b). A reversal of polarity in the TRFs seems to exist at an azimuth of 160°. However, the pattern is not much clear for the poor coverage. The AWST section in Figure 3d shows a clear pattern of anisotropy. We estimated the FD at 160° azimuth using the maximum amplitudes (Shen
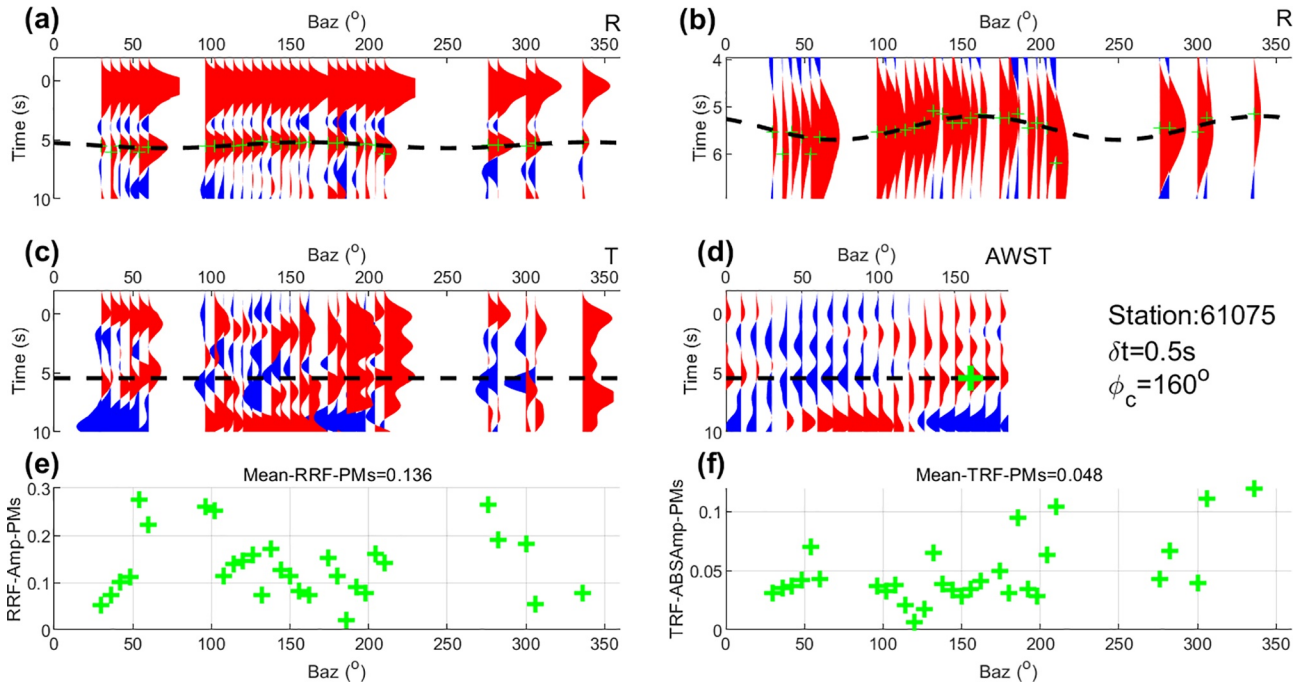
Figure 3. Observed receiver functions and azimuth-weighted stacking of TRF (AWST) section of station 61075. (a) R component of receiver functions (RRFs). Thin green pluses symbols mark the P-to-S (P_Ms) arrivals. The black dashed line marks the arrival of the P_Ms phase predicted by the anisotropic model. (b) Zoomed-in RRFs in a narrow time window to highlight the variation of the P_Ms arrivals. The black-dashed line marks the arrival of the P_Ms phase predicted by the anisotropic model. (c) T component of receiver functions (TRFs). The black-dashed line marks the average value of the P_Ms arrivals. The green plus marks the location of the azimuth related to the FD of the anisotropic layer determined by the AWST section in Figure 2d. (d) AWST section. The green plus marks the azimuth of the maximum stacking amplitude from the lower interface, which corresponds to the fast direction (FD) of the anisotropic layer. The black dashed line marks the average value of the P_Ms arrival. The station name, split time (δt), and FD (ø$_c$) are also marked. (e) The amplitude variation of RRFs in different azimuthal intervals. Mean-RRF-P_Ms indicates the average of all RRFs amplitudes. (f) The absolute amplitude variation of TRFs in different azimuthal intervals. Mean-TRF-P_Ms indicates the absolute amplitudes of all TRFs amplitudes.

et al., 2015). Finally, the anisotropy parameters of the crust below the station were obtained: the delay time was 0.11s and the FD was 160°. The results of the FD from RRFs and TRFs are consistent, which implies further reliability.

Figure 4 indicates the results for station 15705, which is a kind of station with 2π periodicity of arrivals of P_Ms against back azimuth, which implies a single layer of anisotropy with a tilted symmetry axis. In the present study, there were 17 stations with a period rule of 2π, which are represented by a yellow triangle in Figure 1a. There were 201 RRFs and TRFs in the station 15705. We determined the delay time and the FD by fitting the arrivals of P_Ms with a periodicity of 2π caused by the anisotropic layer of the inclined symmetry axis, as shown in Figure 4.

3. Results and Discussions

3.1. Crustal Anisotropy

Following the same data processing as in Section 2, we obtained the anisotropic results for all the 87 stations. The results for all other stations are shown in Figure S1, and the parameters of crustal anisotropy are listed in Table S1 and are provided as supplementary materials. Figure 5 indicates the distribution of crustal anisotropy in the study area. The results indicate that the main fast directions of the anisotropic layer were N-S and NE-SW, with delay times of 0.01–1.34 s as shown by the red rose diagram in Figure 5.

Recently, an increasing number of scholars have used receiver function to obtain anisotropy, mainly using the Moho Ps phase splitting to estimate bulk crustal anisotropy (Liu & Niu, 2012; Z. Liu et al., 2015; Niu et al., 2016; Shen et al., 2015; Sun et al., 2015). Scholars have developed an integrated technique for estimating crustal anisotropy that could be applied to any broadband seismic stations having a good backazimuthal
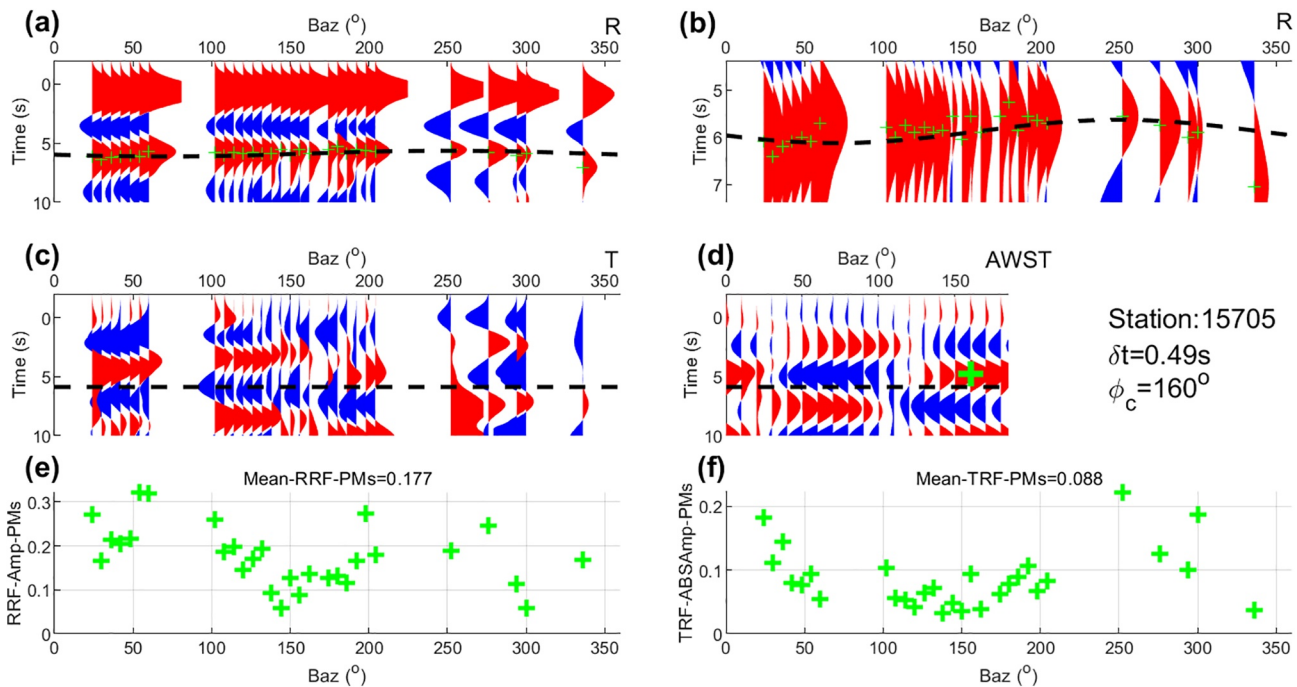
Figure 4. Same as Figure 3 except for station 61075.

Figure 5. Map of anisotropy in the crust. White lines represent the block boundary. The lengths of the blue line indicate the delay times, and their orientations represent the fast axis directions. The rose diagrams correspond to the fast wave directions in a different regions. The red rose diagram shows the results of all stations (Equal-area project rose diagram of the fast direction of all selected events).

coverage of teleseismic events (Liu & Niu, 2012). Sun et al. (2015) estimated the crustal structure and deformation under the Longmenshan and its surroundings by analyzing the receiver function data. Liu and Park (2016) studied the trade-offs between thin anisotropic layers and Ps splitting for crustal anisotropy, and outlined the criteria for choosing one over the other by using a harmonic-decomposition technique. However, certain scholars argue that this approach to anisotropy is unreliable (Brownlee et al., 2017; Lamarque & Agostinetti, 2020), because the Ps splitting paradigm requires a strongly anisotropic thick crust to generate sufficient birefringence to explain the RFs. However, very large back azimuth amplitude variations in the Ps converted phase can be generated with relatively thin anisotropic layers (Z. Liu et al., 2015).

In order to discuss the depth of the anisotropic layer, we constructed different crust models to compare the observations corresponding to the anisotropy parameters of station 61075. Figures 6a–6d exhibit the models with anisotropic layer within the whole crust, upper crust, mid-crust, and lower crust. The total anisotropic strength (thickness × percent anisotropy) of all models is the same. The corresponding synthetic receiver functions are shown in Figure 7. The results indicate that the thin anisotropic layer in the lower crust can generate a comparable pattern of $P_{M}s$ arrivals by back azimuth on radial receiver functions. Another useful piece of information is the amplitude of $P_{M}s$ on radial and transverse receiver functions, as shown in Figure 8. The amplitudes of $P_{M}s$ on the radial receiver functions are not sensitive to the depth of the anisotropic layer, while the amplitudes of $P_{M}s$ on the transverse component are a little sensitive to the depth of the anisotropic layer. Especially, the amplitude of $P_{M}s$ on the transverse component with a thin anisotropic layer above the Moho is evidently larger than those in the other models. We also selected the amplitudes of the observations of station 61075 and compared them with
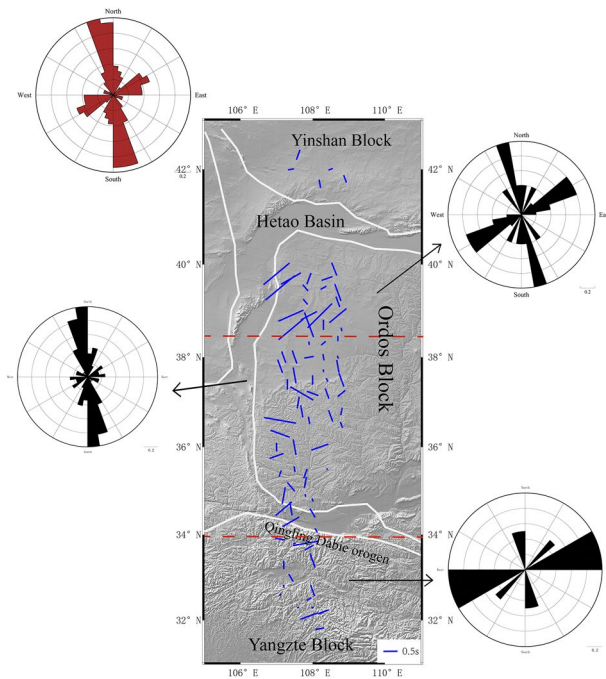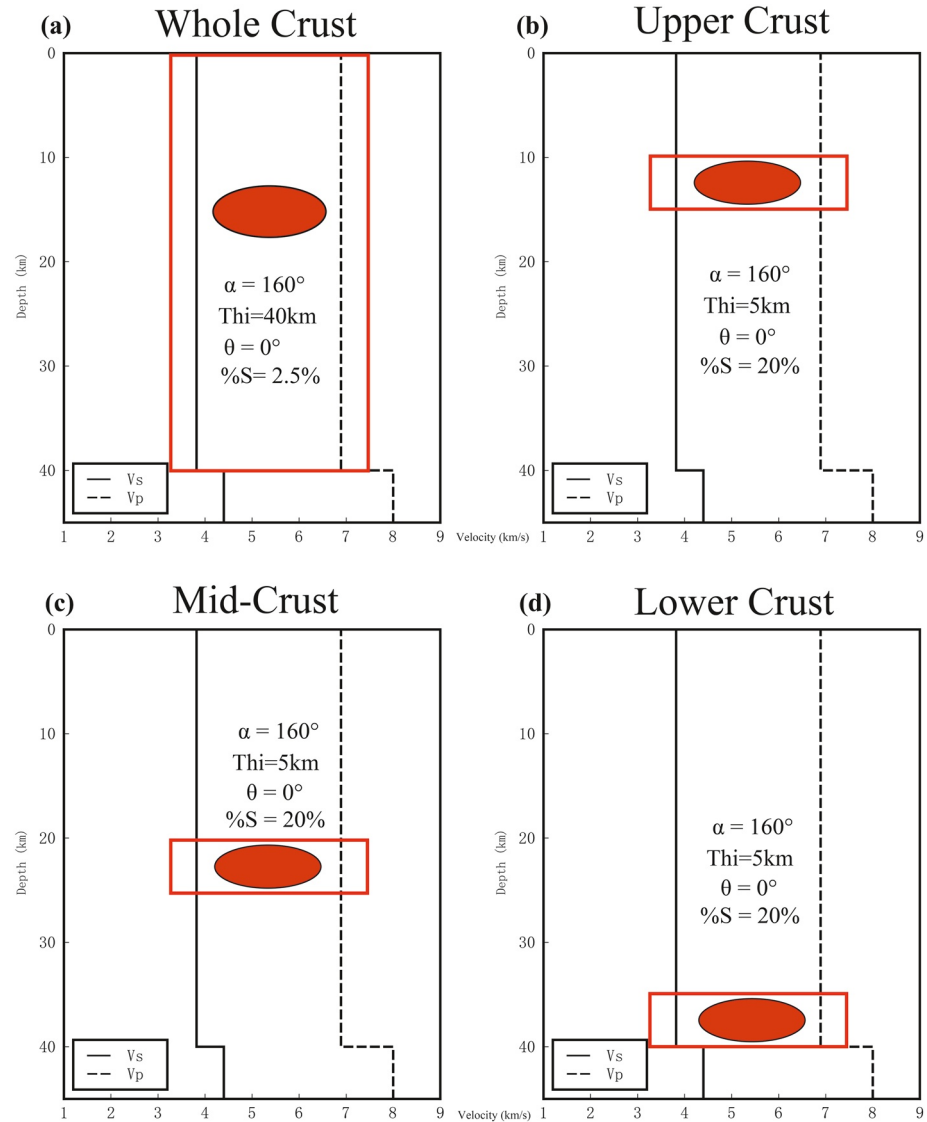
Figure 6. The crust models with anisotropic layer at different depths. The red box indicates the position of the anisotropic layer in the crust. Figures a–d depicts the anisotropic layer models of the whole crust, upper crust, middle crust, and lower crust, respectively. The %S value indicates the anisotropic strength, and α and θ indicate the strike and inclination of the fast axis, respectively. "Thi" represents the thickness of the anisotropic layer.

the synthetics (Figure 8), which revealed that the amplitude of the model with a thin anisotropic layer above the Moho was consistent with the observations. We also investigated the amplitudes of all stations (refer to supplement) and observed that the average $P_M s$ amplitude on the radial receiver functions is about 0.125 and that on the transverse component is 0.056. So, our results might represent the anisotropy in the lower crust.

Nonetheless, the actual situation of deep earth anisotropy must be further complicated because of three-dimensional heterogeneity or multi-layer anisotropy. Here, we have obtained only the information of crustal anisotropy in one way, and the results indicated the distinct and meaningful features of local crustal anisotropy by analyzing a large amount of receiver function data recorded by the dense broadband seismic array. According to our results, the orientation of the anisotropic fast axis is probably more robust than the
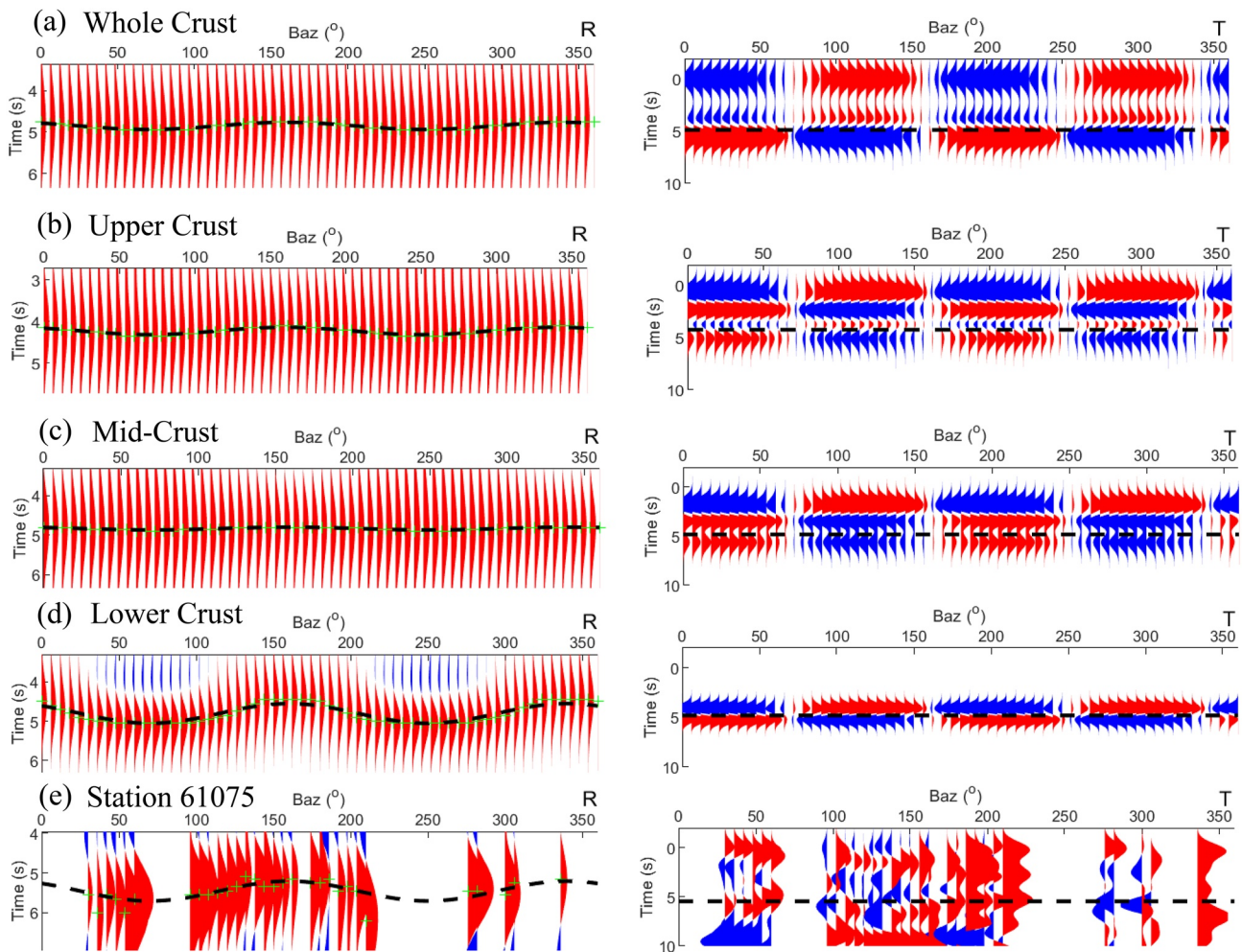
Figure 7. Synthetic receiver functions. (a–d) are the synthetic R component of receiver functions (RRFs) and T component of receiver functions (TRFs) of models in Figure 6. (e) Observed RRFs and TRFs of station 61075.

inferred splitting time because the back-azimuthal patterns for the models with anisotropic layers at different depths are similar. So, we will only discuss the fast-axis orientation of our results.

As the distribution of the fast direction has evident local features, we divided the research area into three parts: the north Ordos including Yinshan Block, south Ordos, and Yangtze Block (Figure 5). In the north Ordos and Yinshan block, the dominant orientation of the fast axis is NEE-SSW, with a delay time of 0.13–1.34 s. In the south Ordos block, the dominant orientation of the fast axis is N-S, with a delay time of 0.01–1.15 s. In Qingling-Dabie orogen, the dominant orientation of the fast axis is E-W, with the delay time of 0.08–0.68 s.

3.2. The Geodynamic Process Imprinted by Crustal Anisotropy

The fast-axis orientations of the crustal anisotropy in different regions were agreeable, which should be related to the major geological events. The NEE-SWW dominant orientation in north Ordos and Yinshan block could be correlated to the Paleoproterozoic (~1.95 Ga) continent-to-continent collision between the Ordos Block in the south and the Yinshan Block in the north, which resulted in a NE-SW-trending linear crustal belt and the final amalgamation of the uniform Western Block (Gou et al., 2018;
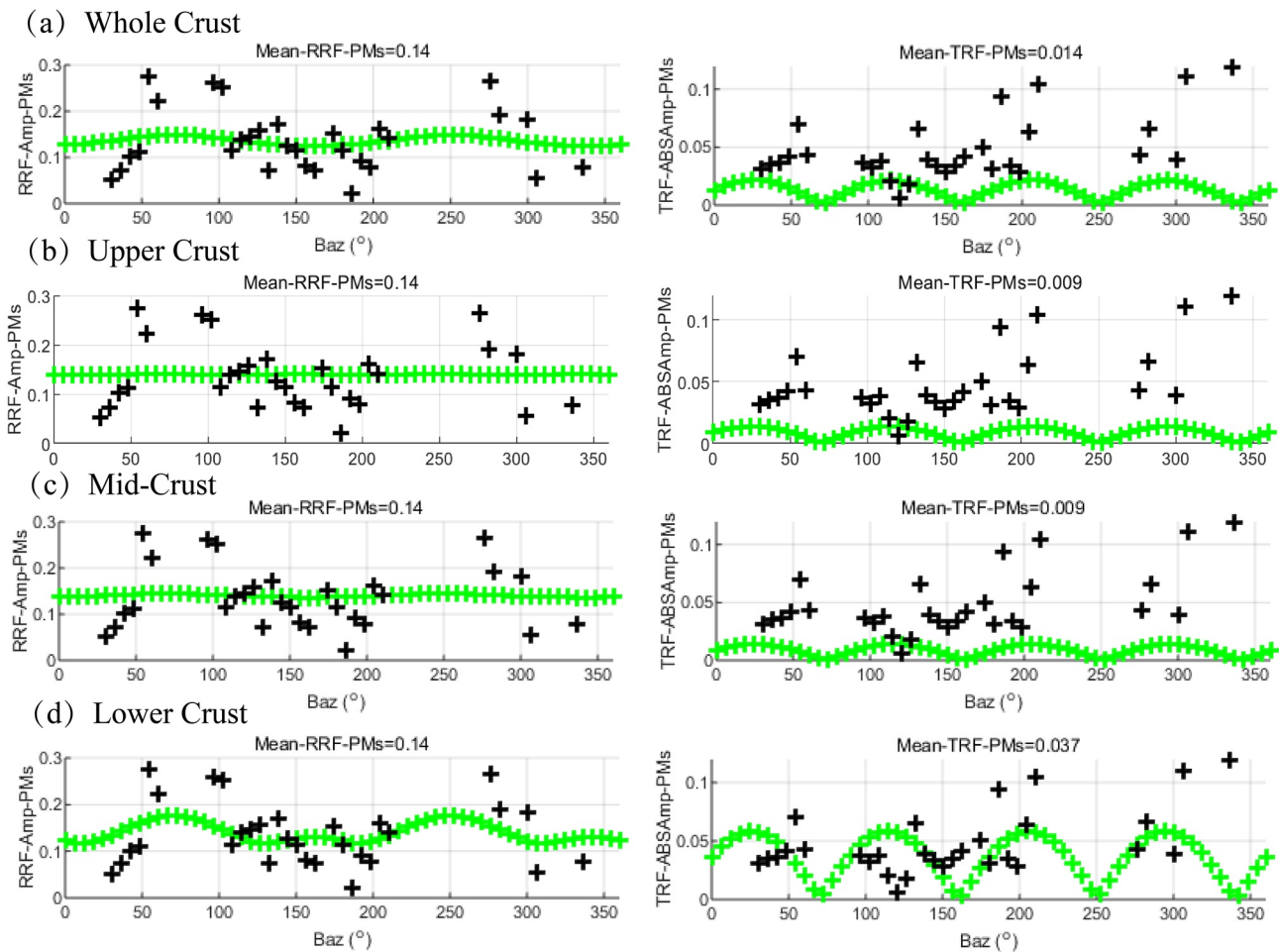
(a) Whole Crust

(b) Upper Crust

(c) Mid-Crust

(d) Lower Crust

Figure 8. The amplitude of P-to-S (P_{M}s) on R component of receiver functions (RRFs) and T component of receiver functions (TRFs). The green plus symbols the absolute amplitudes of the P_{M}s on RRFs and TRFs (Figure 7) corresponding to the different models in Figure 6. The black plus indicates the amplitude of station 61075.

Wan et al., 2020; X. Wang et al., 2019; Yin et al., 2011; Zhao & Zhai, 2013). The other group of N-S anisotropy in the south Ordos is most likely related to the collision between the Western Block (including Ordos and Yinshan Blocks) and Eastern Block ~1.85 Ga. This ultimately formed the uniform basement of the North China Craton along the N-S-trending Crustal-scale Trans-North China Orogen (Zhao & Zhai, 2013). Some sporadic N-S anisotropy in the north Ordos might also be attributed to this. The E-W dominant anisotropy in Qinling–Dabie orogen is parallel to that in the orogenic belt, which could be caused by the collision between the NCC and the South China Craton in the Triassic (S. Li et al., 1993; Wu et al., 2009).

In addition, the crust thickness of the Ordos block is about 44 km (W. L. Wang et al., 2017), which is thicker than the normal continental crust of 33 km. So, the Ordos block is more likely to sustain a ductile lower layer, which might be the main reason for the crustal anisotropy observed in our results. In order to visually display the relationship between the formation of crustal anisotropy and the deformation of crust and mantle during the tectonic process, we made cartoons, as shown in Figure 9, illustrating the possible geological events related to the crustal anisotropy in different regions of Ordos block and its adjacent regions.
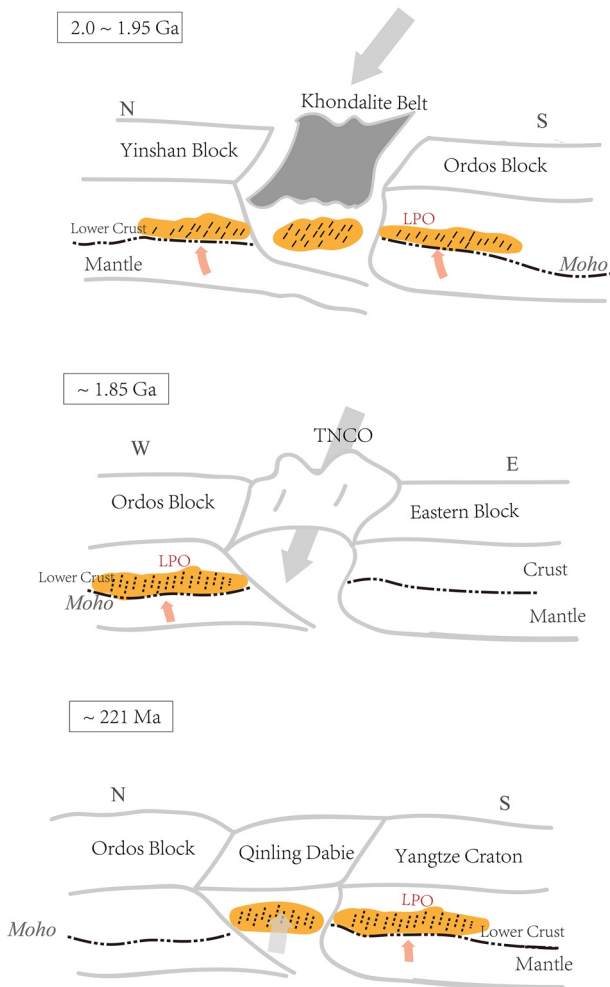
Figure 9. Cartoon of tectonic evolution and crust anisotropy. Diagram for the anisotropy of ancient fossils that may have been caused by different ages, chronological reference (Wu et al., 2009; Zhao & Zhai, 2013). TNCO: Trans-North China Orogen. The gray arrow indicates the extension and deformation direction of the block. The yellow area shows the elevation of the lower crust due to tectonic impact, and the black dotted line shows the direction of the LPO (Barruol & Mainprice, 1993).

3.3. Interaction of Crust and Mantle

Based on the previous studies on the Ordos block and its adjacent areas, it is generally observed that the delay time of crustal contribution is smaller than that of the SKS/XKS acquisitions (Chang et al., 2011; Sherrington et al., 2004; Weeraratne et al., 2009). In addition, the lower mantle is considered to be isotropic (Savage, 1999). Therefore, it is generally believed that the anisotropy measured by the SKS splitting mainly represents the anisotropy of the upper mantle. So, we can discuss the interaction of crust and mantle according to our results and SKS splitting.

Chang et al. (2017) used the XKS method to obtain the upper mantle anisotropy results in this region with the same data set as shown in Figure 10. The results showed that the delay time of the Qingling-Dabie orogen belt in the southern margin of the Ordos block is large, with an average of about 1.3 s, and the dominant orientation is near the E-W direction. The dominant fast axis orientation inside Ordos block is near the N-S direction in the north and near the E-W direction in the south, with a relatively weak anisotropy throughout the Ordos. The translucent rectangles in Figure 10 depict the dominant fast axis orientations from SKS and receiver functions. The results indicated that the fast axis orientation of crust and upper mantle in the south Ordos block is nearly perpendicular, which implies the decoupling of crust and mantle. The good consistency of fast axis orientation in the Qinling–Dabie orogen belt indicates the coupling of crust and mantle. The fast axis orientation of crust and upper mantle in the north Ordos is neither perpendicular nor parallel, which indicates a relatively complicated interaction of crust and mantle.

Based on the results of SKS splitting, Yu and Chen (2016) documented that the dominant orientation of the upper mantle material migration in the south Ordos block and Qingling-Dabie orogen belt is E-W, which might be caused by the Tibetan Plateau squeezing "out" eastward. Referring to the large delay time of SKS splitting, Chang et al. (2017) deduced that the SKS splitting in the south Ordos block and Qingling-Dabie orogen belt could be mainly contributed by the material migration from the Tibetan plateau, besides the collision between the North China block and the South China block, which led to the extension and deformation of the crust to the lithospheric mantle along the E-W direction. Our results indicated that the fast axis orientation in the south Ordos is apparently different from that in the Qinling–Dabie orogen belt. In addition, the results from the dense GPS velocity field across the Ordos block indicated that the interior of the block undergoes no differential motion and its internal strain is insignificant (Hao et al., 2021), which imply that the mantle from the west has little influence on the NS-trending anisotropy beneath the south Ordos block.

The Ordos block has been considered as a stable Archean continental block (An & Shi, 2006) with the medium related to feldspar lithology in the lower crust (C. Y. Liu et al., 2006). However, some results from recent studies indicate that the crust of the Ordos block is not totally consistent with the typical craton crust with a lower Vp/Vs ratio. For example, results from the receiver functions indicate that the thickness of the crust decreased significantly when the latitude was larger than 38° (L. T. Huang et al., 2020). The northern part of the Ordos block is characterized by a larger velocity jump as well as
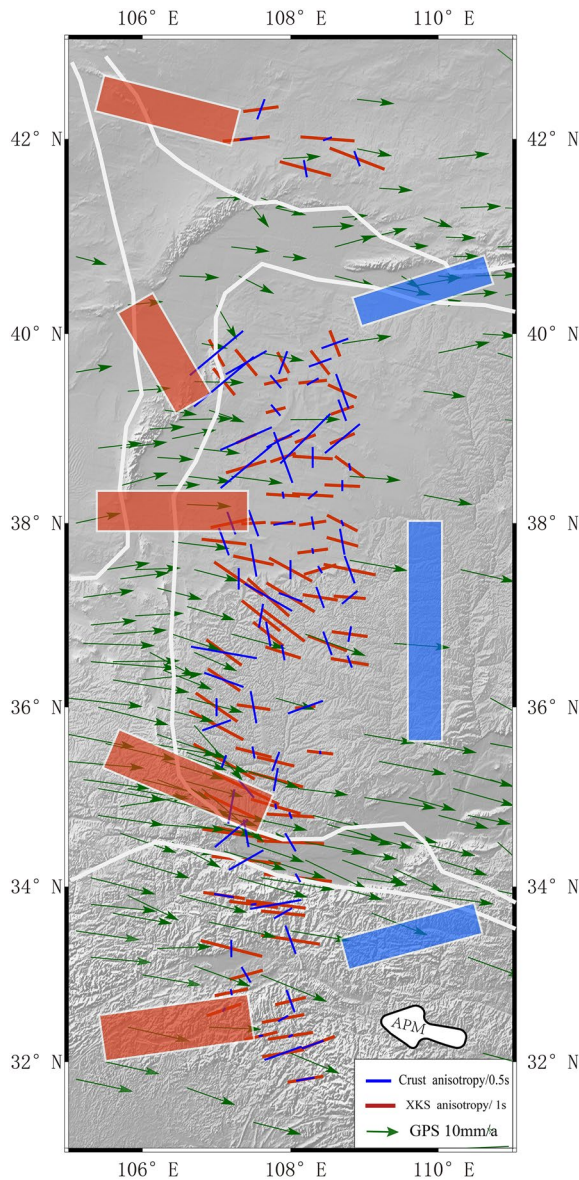
Figure 10. Comparison of the crustal anisotropy with the results from XKS. Blue lines: the fast direction (FD) of crust anisotropy observed in this study. Red lines: the XKS results (Chang et al., 2017). Green arrows: GPS results (Niu et al., 2005). The white arrow indicates the absolute plate motion (APM) direction. The red and the blue translucent rectangles represent the dominant fast wave directions of anisotropy in the upper mantle and the crust in different regions.

a large Vp/Vs ratio (Figure 11), indicating that the crust beneath the station to be a mafic rock (W. L. Wang et al., 2017). Previous results (H. Dong et al., 2014; H. L. Guo et al., 2017; Tian et al., 2011) from tomography studies documented that an evident low-velocity anomaly existed in the lower crust and the upper mantle from the north of Ordos block to the Hetao basin. It is speculated that an upwelling mantle material might exist under the north Ordos block. The upwelling mantle material has invaded the crust of the northern Ordos from north to south, and caused the partial melt of the lower crust, Moho uplift, a higher Vp/Vs ratio, and a larger velocity jump of Moho. The fusion of mantle material and crustal material might also lead to a decrease in the density jump, as mentioned by L. T. Huang et al. (2020). The distinct difference in the fast axis orientation of the crustal anisotropy in the north Ordos block could also be contributed to the immersion and modification of the upwelling mantle.

Based on the previous results and the results of the crustal anisotropy, we present a simplified sketch of the geodynamic model in the west Ordos block and its adjacent regions (Figure 12). The Qinling–Dabie orogen belt is a contrasting boundary of crustal anisotropy of South China block and North China block. Another prominent feature of the model is the upwelling of the mantle material in north Ordos block and the horizontal flow of the mantle material in south Ordos block. Especially, the upwelling mantle material led to the partial melt of the lower crust, Moho uplift, the decrease in the density jump, and the distinct difference of the fast wave direction of crustal anisotropy in the north Ordos block.

Combined with the results of previous studies (Chang et al., 2017; H. Dong et al., 2014; H. L. Guo et al., 2017; L. T. Huang et al., 2020), the results of the present study indicate that the partial melting in the north of Ordos block might be caused by thermal erosion, resulting in slow crust subsidence. It is also a sign that the north of the Ordos block may be experiencing very slow craton destruction.

4. Conclusions

Based on the numerous observations from the 87 broadband seismic stations of Chin Array-Himalaya II seismic array in the Ordos block, we determined the crust anisotropic parameters of the block and its adjacent areas using radial and tangential receiver functions. According to the numerical tests and the amplitudes of the observed receiver functions, we deduced that the anisotropy is been mainly contributed by the lower crust.

The results indicated the distinct difference in the dominant fast axis orientation of the north Ordos block, south Ordos block, and Qinling–Dabie orogen belt. The crustal anisotropy could be related to major geological events. The NEE-SSW dominant orientation in north Ordos and Yinshan block could be correlated to the Paleoproterozoic continent-to-continent collision between the Ordos Block and the Yinshan Block. The N-S anisotropy in the south Ordos is most likely related to the collision between the Western Block and Eastern Block of the North China Craton. The E-W dominant anisotropy in Qinling–Dabie orogen could be mainly attributed to the material migration from the Tibetan plateau in Cenozoic, although the collision between the North
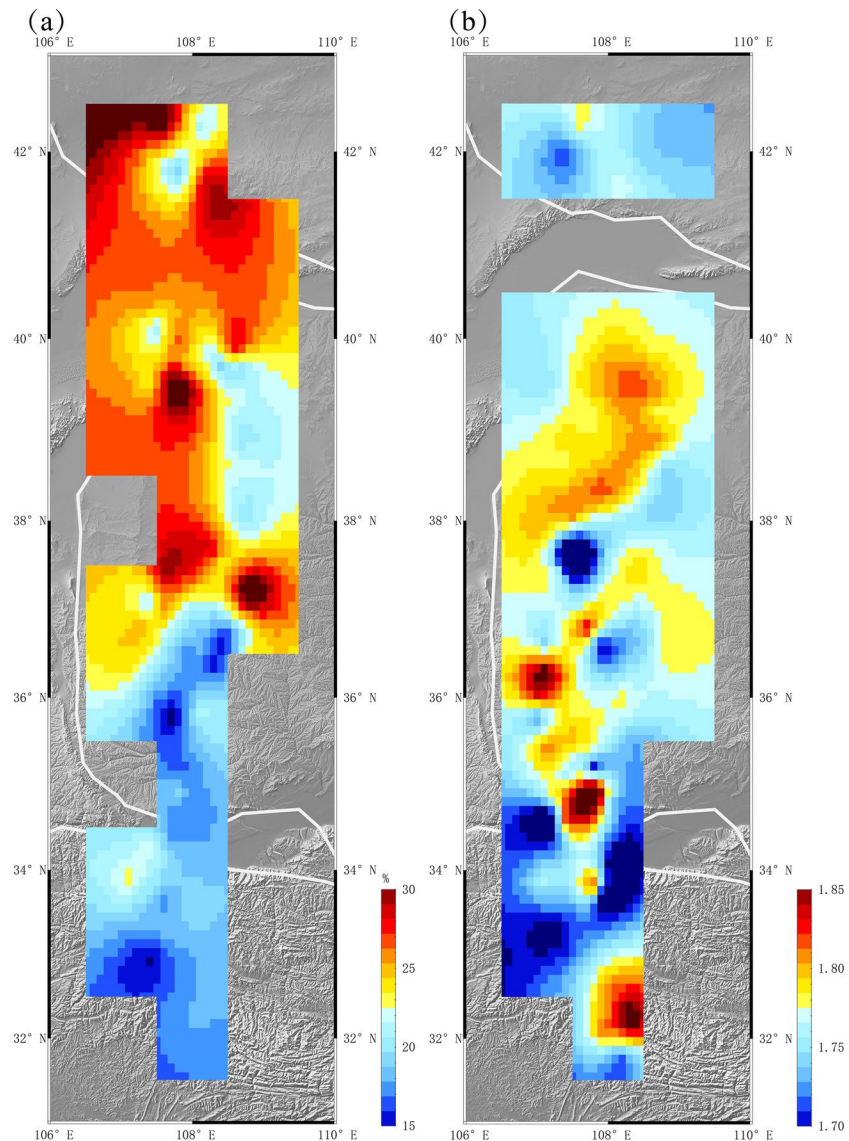
Figure 11. (a) Results of velocity contrast across Moho (L. T. Huang et al., 2020) and (b) the crustal Vp/Vs ratio (W. L. Wang et al., 2017) in this study region.

China block and the South China block in the Triassic could also play a similar role. So, it was inferred that the traces of ancient tectonic movements are still preserved by the crustal anisotropy within the Ordos block.

According to the results from the analysis of tomography, crustal velocity ratio, crustal thickness, and Moho features, we observed the contrasting structures beneath the north and south Ordos blocks. The evident low-velocity abnormalities, larger velocity ratios, and a distinct Moho velocity jump indicated the partial melting in the upper mantle in the north Ordos block, which implies the upwelling of mantle material. Based on this, we deduced that the north Ordos block might currently be experiencing craton destruction. The remarkable differences in the interior structures of north and south Ordos blocks could mainly be attributed to the different movement of the mantle material.
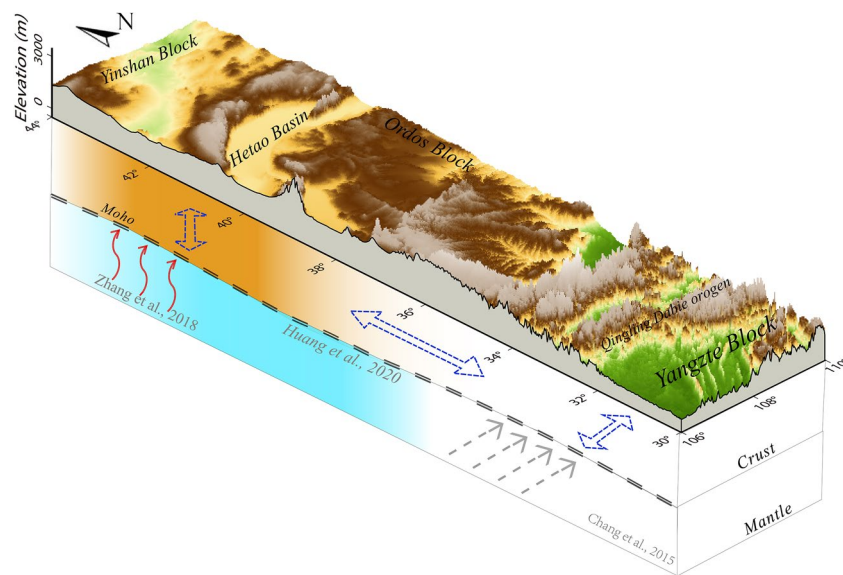
Figure 12. Crust-mantle interaction model. The orange part represents the crustal model, and the deeper color represents the high values of the crustal velocity ratio (W. L. Wang et al., 2017). The blue part represents the mantle model, and the lighter color represents a smaller density jump (L. T. Huang et al., 2020). The black double dashed line represents the Moho boundary between the crust and the mantle. The Blue dashed arrow indicates the FD of the crust. The Gray dashed line represents the squeeze from the Tibetan Plateau. The red arrow indicates the upwelling of hot materials (Zhang et al., 2018).

Data Availability Statement

Raw receiver functions of this article can be found online at https://doi.org/10.5281/zenodo.4899075.

References

An, M., & Shi, Y. (2006). Lithospheric thickness of the Chinese continent. *Physics of the Earth and Planetary Interiors*, *159*(3–4), 257–266. https://doi.org/10.1016/j.pepi.2006.08.002

Bar, N., Long, M. D., Wagner, L. S., Beck, S. L., Zandt, G., & Tavera, H. (2019). Receiver function analysis reveals layered anisotropy in the crust and upper mantle beneath southern Peru and northern Bolivia. *Tectonophysics*, *753*, 93–110. https://doi.org/10.1016/j.tecto.2019.01.007

Barruol, G., & Mainprice, D. (1993). 3-D seismic velocities calculated from lattice-preferred orientation and reflectivity of a lower crustal section: Examples of the Val Sesia section (Ivrea zone, northern Italy). *Geophysical Journal International*, *115*(3), 1169–1188. https://doi.org/10.1111/j.1365-246x.1993.tb01519.x

Brownlee, S. J., Schulte-Pelkum, V., Raju, A., Mahan, K., Condit, C., & Orlandini, O. F. (2017). Characteristics of deep crustal seismic anisotropy from a compilation of rock elasticity tensors and their expression in receiver functions. *Tectonics*, *36*, 1835–1857. https://doi.org/10.1002/2017TC004625

Chang, L. J., Ding, Z. F., Wang, C. Y., & Flesch, L. M. (2017). Vertical coherence of deformation in lithosphere in the NE margin of the Tibetan plateau using GPS and shear-wave splitting data. *Tectonophysics*, *699*, 93–101. https://doi.org/10.1016/j.tecto.2017.01.025

Chang, L. J., Wang, C. Y., & Ding, Z. F. (2011). Upper mantle anisotropy in the Ordos block and its margins. *Science China Earth Sciences*, *54*, 888–900. https://doi.org/10.1007/s11430-010-4137-2

Crampin, S. (1987). Geological and industrial implications of extensive-dilatancy anisotropy. *Nature*, *328*(6130), 491–496. https://doi.org/10.1038/328491a0

Deng, Q. D., Cheng, S. P., Min, W., Yang, G. Z., & Reng, D. W. (1999). Discussion on Cenozoic tectonics and dynamics of Ordos block. *Journal of Geomechanics*, *5*(3), 13–21. https://doi.org/10.1023/a:1005186016971

Dong, H., Wei, W. B., Ye, G. F., Jin, S., Jones, A. G., Jing, J. N., et al. (2014). Three-dimensional electrical structure of the crust and upper mantle in Ordos block and adjacent area: Evidence of regional lithospheric modification. *Geochemistry, Geophysics, Geosystems*, *15*(6), 2414–2425. https://doi.org/10.1002/2014GC005270

Dong, Y. P., & Santosh, M. (2016). Tectonic architecture and multiple orogeny of the Qinling Orogenic Belt, Central China. *Gondwana Research*, *29*, 1–40. https://doi.org/10.1016/j.gr.2015.06.009

Frederiksen, A. W., & Bostock, M. G. (2010). Modelling teleseismic waves in dipping anisotropic structures. *Geophysical Journal of the Royal Astronomical Society*, *141*(2), 401–412.

Gan, W., Zhang, P., Shen, Z. K., Niu, Z., Wang, M., Wan, Y., et al. (2007). Present-day crustal motion within the Tibetan Plateau inferred from GPS measurements. *Journal of Geophysical Research*, *112*, B08416. https://doi.org/10.1029/2005JB004120

Gou, L., Li, Z., Liu, X., Dong, Y., Zhao, J., Zhang, C., et al. (2018). Ultrahigh-temperature metamorphism in the Helanshan complex of the Khondalite belt, North China craton: Petrology and phase equilibria of spinel-bearing pelitic granulites. *Journal of Metamorphic Geology*, *36*(9), 1199–1220.

Guo, B., Liu, Q. Y., Chen, J. H., Zhao, D. P., Li, S. C., & Lai, Y. G. (2004). Seismic tomographic imaging of the crust and upper mantle beneath the northeastern edge of the Qinghai-Xizang plateau and the Ordos area. *Chinese Journal of Geophysics*, *47*(5), 790–797. (in Chinese). https://doi.org/10.1002/cjg2.566

Guo, H. L., Ding, Z. F., & Xu, X. M. (2017). Upper mantle structure beneath the northern South-North Seismic Zone from teleseismic traveltime data. *Chinese Journal of Geophysics*, *60*(1), 86–97. (in Chinese). https://doi.org/10.6038/cjg20170108

Hao, M., Wang, Q., Zhang, P., Li, Z., Li, Y., & Zhuang, W. (2021). "Frame wobbling" causing crustal deformation around the Ordos block. *Geophysical Research Letters*, *48*, e2020GL091008. https://doi.org/10.1029/2020GL091008

Huang, L. T., Shen, X., Zheng, W. J., Qian, Y. P., Zhang, D. L., Wang, W. T., & Ii, X. L. (2020). Moho properties of western Ordos block and surrounding regions constrained by teleseismic receiver functions and its tectonic implication. *Chinese Journal of Geophysics*, *63*(3). (in Chinese). https://doi.org/10.6038/cjg2020N0210

Huang, Z., Xu, M., Wang, L., Mi, N., Yu, D., & Li, H. (2008). Shear wave splitting in the southern margin of the Ordos block, north China, Geophysical Research. *Letters*, *35*(19). https://doi.org/10.1029/2008gl035188

Jia, M., Wang, X. G., Li S L., & Chen, Y. S. (2015). Crustal structures of Ordos block and surrounding regions from receiver functions. *Progress in Geophysics*, *30*(6), 2474–2481. https://doi.org/10.6038/pg20150605

Jia, S. X., Wang, F. Y., Tian, X. F., Duan, Y. H., Zhang, J. S., Liu, B. F., & Lin, J. Y. (2014). Crustal structure and tectonic study of North China Craton from a long deep seismic sounding profile. *Tectonophysics*, *627*, 48–56. https://doi.org/10.1016/j.tecto.2014.04.013

Kusky, T. M. (2011). Comparison of results of recent seismic profiles with tectonic models of the north China craton. *Journal of Earth Science*, *22*, 250–259. https://doi.org/10.1007/s12583-011-0178-5

Lamarque, G., & Agostinetti, N. P. (2020). Modeling of anisotropy in the lithosphere and asthenosphere for real Earth cases: A critical assessment of the impact on SKS measurements. *Journal of Geophysical Research: Solid Earth*, *125*. https://doi.org/10.1029/2019JB018978

Li, S., Xiao, Y., Liou, D., Chen, Y., Ge, N., & Zhang, Z. (1993). Collision of the North China and Yangtse Blocks and formation of coesitebearing eclogites: Timing and processes. *Chemical Geology*, *109*(1–4), 89–111. https://doi.org/10.1016/0009-2541(93)90063-o

Li, S. L., Zhang, X. K., Zhang, C. K., Zhao, J. R., & Cheng, S. X. (2002). A preliminary study on the crustal velocity structure of Maqin–Lanzhou–Jingbian by means of deep seismic sounding profile. *Chinese Geophysics*, *45*, 210–217. https://doi.org/10.1002/cjg2.233

Li, W. P., Liu, S F., Tao, Q., Dou, G. X., & Gao, T. J. (2014). Analysis of structural deformation in the North Dabashan thrust belt, South Qinling, central China. *International Geology Review*, *56*, 1276–1294. https://doi.org/10.1080/00206814.2014.935966

Ligorria, J. P., & Ammon, C. J. (1999). Iterative deconvolution and receiver-function estimation. *Bulletin of the Seismological Society of America*, *89*(5), 1395–1400.

Liu, C. Y., Zhao, H. G., Gui, X. J., Yue, L. P., Zhao, J. F., & Wang, J. Q. (2006). Space-time coordinate of the evolution and reformation and mineralization response in Ordos Basin. *Acta Geologica Sinica*, *80*, 617–638.

Liu, H., & Niu, F. (2012). Estimating crustal seismic anisotropy with a joint analysis of radial and transverse receiver function data. *Geophysical Journal International*, *188*, 144–164. https://doi.org/10.1111/j.1365-246x.2011.05249.x

Liu, Z., & Park, J. (2016). Seismic receiver function interpretation: Ps splitting or anisotropic underplating? *Geophysical Journal International*, *208*, 1332–1341. https://doi.org/10.1093/gji/ggw455

Liu, Z., Park, J., & Rye, D. M. (2015). Crustal anisotropy in northeastern Tibetan Plateau inferred from receiver functions: Rock textures caused by metamorphic fluids and lower crust flow? *Tectonophysics*, *661*, 66–80. https://doi.org/10.1016/j.tecto.2015.08.006

Long, M. D. (2013). Constraints on subduction geodynamics from seismic anisotropy. *Reviews of Geophysics*, *51*, 76–112. https://doi.org/10.1002/rog.20008

Long, M. D., & Silver, P. G. (2009). Shear wave splitting and mantle anisotropy: Measurements, interpretations, and new directions. *Surveys in Geophysics*, *30*, 407–461. https://doi.org/10.1007/s10712-009-9075-1

Mccormack, K., Wirth, E. A., & Long, M. D. (2013). B-type olivine fabric and mantle wedge serpentinization beneath the Ryukyu arc. *Geophysical Research Letters*, *40*(9), 1697–1702. https://doi.org/10.1002/grl.50369

Niu, X., Zhao, D., Li, J., & Ruan, A. (2016). P wave azimuthal and radial anisotropy of the Hokkaido subduction zone. *Journal of Geophysical Research: Solid Earth*, *121*, 2636–2660. https://doi.org/10.1002/2015JB012651

Niu, Z. J., Wang, M., & Sun, H. (2005). Contemporary velocity field of crustal movement of Chinese mainland from global positioning system measurements. *Chinese Science Bulletin*, *50*(9), 939–941. https://doi.org/10.1360/982005-220

Savage, M. K. (1999). Seismic anisotropy and mantle deformation: What have we learned from shear wave splitting? *Reviews of Geophysics*, *37*(1), 65–106. https://doi.org/10.1029/98RG02075

Shen, X. Z., Yuan, X. H., & Ren, J. S. (2015). Anisotropic low-velocity lower crust beneath the northeastern margin of Tibetan Plateau: Evidence for crustal channel flow. *Geochemistry, Geophysics, Geosystems*, *16*, 12–4236. https://doi.org/10.1002/2015GC005952

Sherrington, H. F., Zandt, G., & Frederiksen, A. W. (2004). Crustal fabric in the Tibetan Plateau based on waveform inversions for seismic anisotropy parameters. *Journal of Geophysical Research*, *109*, B02312. https://doi.org/10.1029/2002JB002345

Silver, P. G. (1996). Seismic anisotropy beneath the continents: Probing the depths of geology. *Annual Review of Earth and Planetary Sciences*, *24*(1), 385–432. https://doi.org/10.1146/annurev.earth.24.1.385

Silver, P. G., & Chan, W. W. (1991). Shear wave splitting and subcontinental mantle deformation. *Journal of Geophysical Research*, *96*(B10), 16429–16454. https://doi.org/10.1029/91jb00899

Sun, Y., Liu, J., Zhou, K., Chen, B., & Guo, R. (2015). Crustal structure and deformation under the Longmenshan and its surroundings revealed by receiver function data. *Physics of the Earth and Planetary Interiors*, *244*, 11–22. https://doi.org/10.1016/j.pepi.2015.04.005

Tian, X. B., Teng, J. W., Zhang, H. S., Zhang, Z. J., Zhang, Y. Q., Yang, H., & Zhang, K. (2011). Structure of crust and upper mantle beneath the Ordos block and the Yinshan Mountains revealed by receiver function analysis. *Physics of the Earth and Planetary Interiors*, *184*(3), 186–193. https://doi.org/10.1016/j.pepi.2010.11.007

Wan, B., Yang, X. S., Tian, X. B., Yuan, H. Y., Kirscher, U., & Mitchell, R. N. (2020). Seismological evidence for the earliest global subduction network at 2 Ga ago. *Science Advances*, *6*, eabc5491. https://doi.org/10.1126/sciadv.abc549

Wang, W. L., Wu, J. P., Fang, L. H., Lai, G. J., & Cai, Y. (2017). Sedimentary and crustal thicknesses and Poisson's ratios for the NE Tibetan Plateau and its adjacent regions based on dense seismic arrays. *Earth and Planetary Science Letters*, *462*, 76–85. https://doi.org/10.1016/j.epsl.2016.12.040

Wang, X., Li, X. P., Zhang, J., & Schertl, H. P. (2019). Geochemistry, geochronology and evolution of Paleoproterozoic granitoid gneisses in the Khondalite Belt, North China Craton. *Precambrian Research*, *338*, 105590.

Weeraratne, D. S., Karalliyadda, S., & Silver, P. G. (2009). Very little crustal anisotropy in eastern Tibet from regional S phases, the Game's Over. *Eos, Transactions. AGU. Fall Meeting Supplement Abstract S11A-1690*. Retrieved from https://ui.adsabs.harvard.edu/abs/2009AGUFM.S11A1690W

Wessel, P., & Smith, W. H. F. (1995). New version of the generic mapping tools. *Eos, Transactions - American Geophysical Union*, *76*(33), 329. https://doi.org/10.1029/95EO00198

Wu, Y. B., Hanchar, J. M., Shan, G., Sylvester, P. J., Tubrett, M., Qiu, H. N., et al. (2009). Age and nature of eclogites in the Huwan shear zone, and the multi-stage evolution of the Qinling-Dabie-Sulu Orogen, central China. *Earth and Planetary Science Letters*, *277*(3–4), 345–354. https://doi.org/10.1016/j.epsl.2008.10.031

Yin, C., Zhao, G., Guo, J., Sun, M., Xia, X., Zhou, X., & Liu, C. (2011). U-Pb and Hf isotopic study of zircons of the Helanshan Complex: Constrains on the evolution of the Khondalite Belt in the Western Block of the North China Craton. *Lithos*, *122*, 25–38. https://doi.org/10.1016/j.lithos.2010.11.010

Yu, Y., & Chen, Y. J. (2016). Seismic anisotropy beneath the southern Ordos block and the Qinling-Dabie orogen, China: Eastward Tibetan asthenospheric flow around the southern Ordos. *Earth and Planetary Science Letters*, *455*, 1–6. https://doi.org/10.1016/j.epsl.2016.08.026

Zhang, F., Wu, Q., Li, Y., Zhang, R., Sun, L., Pan, J., & Ding, Z. (2018). Seismic Tomography of Eastern Tibet: Implications for the Tibetan Plateau Growth. *Tectonics*, *37*(9–10), 2833–2847. https://doi.org/10.1029/2018TC004977

Zhao, G. C., & Zhai, M. G. (2013). Lithotectonic elements of Precambrian basement in the North China Craton: Review and tectonic implications. *Gondwana Research*, *23*(4), 1207–1240. https://doi.org/10.1016/j.gr.2012.08.016